Biosensors and Bioelectronics 241 (2023) 115650

Contents lists available at ScienceDirect

Biosensors and Bioelectronics

journal homepage: www.elsevier.com/locate/bios

Soft implantable printed bioelectronic system for wireless continuous monitoring of restenosis

Bruno Rigo [a,b,1], Allison Bateman [a,c,1], Jimin Lee [a,c], Hyeonseok Kim [a,c], Yunki Lee [d,e,f,g], Lissette Romero [a,h], Young C. Jang [d,e,f,g], Robert Herbert [a,c,*], Woon-Hong Yeo [a,c,e,g,**]

[a] IEN Center for Human-Centric Interfaces and Engineering at the Institute for Electronics and Nanotechnology, Georgia Institute of Technology, Atlanta, GA, 30332, USA
[b] School of Electrical and Computer Engineering, Georgia Institute of Technology, Atlanta, GA, 30332, USA
[c] George W. Woodruff School of Mechanical Engineering, Georgia Institute of Technology, Atlanta, GA, 30332, USA
[d] Department of Orthopaedics, Emory Musculoskeletal Institute, Emory University School of Medicine, Atlanta, GA, USA
[e] Wallace H. Coulter Department of Biomedical Engineering, Georgia Institute of Technology and Emory University School of Medicine, Atlanta, GA, 30332, USA
[f] Atlanta VA Medical Center, Decatur, GA, USA
[g] Parker H. Petit Institute for Bioengineering and Biosciences, Institute for Materials, Neural Engineering Center, and Institute for Robotics and Intelligent Machines, Georgia Institute of Technology, Atlanta, GA, 30332, USA
[h] School of Industrial Design, Georgia Institute of Technology, Atlanta, GA, 30332, USA

ARTICLE INFO

Keywords:
Biosensors
Printed sensors
Soft sensors
Vascular electronics

ABSTRACT

Atherosclerosis is a prominent cause of coronary artery disease and broader cardiovascular diseases, the leading cause of death worldwide. Angioplasty and stenting is a common treatment, but in-stent restenosis, where the artery re-narrows, is a frequent complication. Restenosis is detected through invasive procedures and is not currently monitored frequently for patients. Here, we report an implantable vascular bioelectronic device using a newly developed miniaturized strain sensor via microneedle printing methods. A capillary-based printing system achieves high-resolution patterning of a soft, capacitive strain sensor. Ink and printing parameters are evaluated to create a fully printed sensor, while sensor design and sensing mechanism are studied to enhance sensitivity and minimize sensor size. The sensor is integrated with a wireless vascular stent, offering a biocompatible, battery-free, wireless monitoring system compatible with conventional catheterization procedures. The vascular sensing system is demonstrated in an artery model for monitoring restenosis progression. Collectively, the artery implantable bioelectronic system shows the potential for wireless, real-time monitoring of various cardiovascular diseases and stent-integrated sensing/treatments.

1. Introduction

Cardiovascular disease (CVD) is the leading cause of death worldwide, with atherosclerosis being the most frequent cause ("Atherosclerosis - What Is Atherosclerosis?," 2022a). Atherosclerosis is a disease where plaque builds on the inner walls of the arteries and causes a narrowing of the vessels, which restricts blood flow from the heart to other vital organs. This has severe, negative consequences on patients, causing chest pain, heart palpitations, and shortness of breath. Notably, this blood flow restriction increases the risk of heart attacks and stroke ("Atherosclerosis - What Is Atherosclerosis?," 2022b). Atherosclerosis is commonly treated with angioplasty and stenting, where a mesh metal tube called a stent is expanded in the narrowed location of the artery. Using a balloon catheter for minimally invasive deployment, the stent holds open the artery and restores normal blood flow ("Atherosclerosis - Treatment | NHLBI, NIH," 2022). However, a long-term risk of angioplasty is the development of in-stent restenosis, or an overdevelopment of scar tissue where the stent is placed ("Restenosis," n.d.). Although tissue is meant to regrow around a stent to create the proper endothelial lining for smooth blood flow through the vessel, stents also can cause

* Corresponding author. IEN Center for Human-Centric Interfaces and Engineering at the Institute for Electronics and Nanotechnology, Georgia Institute of Technology, Atlanta, GA, 30332, USA.
** Corresponding author. George W. Woodruff School of Mechanical Engineering and IEN Center for Human-Centric Interfaces and Engineering at the Institute for Electronics and Nanotechnology, Georgia Institute of Technology, Atlanta, GA, 30332, USA.
E-mail addresses: rherbert7@gatech.edu (R. Herbert), whyeo@gatech.edu (W.-H. Yeo).
[1] Equally contributed to this work.

https://doi.org/10.1016/j.bios.2023.115650
Received 16 July 2023; Accepted 29 August 2023
Available online 12 September 2023

excessive scar tissue which re-narrows the artery ("Restenosis," n.d.). The likelihood of developing restenosis has decreased significantly, with bare metal stents (BMS) being replaced by drug-eluting stents (DES), from 20 to 40% down to 10% (Cheng et al., 2019). Despite this reduction, bare metal stents are still frequently used as a variety of concerns exist for drug-eluting stents (Alfonso et al., 2014; Stefanini and Holmes, 2013).

There are limited options when diagnosing in-stent restenosis, as it can be asymptomatic until a severe blockage, causing rapid degradation of a patient's condition. Current measurement methods include catheterizations or imaging processes, such as angiography, but such methods are incompatible with frequent or at-home monitoring. Frequent monitoring is important as restenosis progression is highly variable between patients and stent types (Kastrati et al., 2001; Omeh and Shlofmitz, 2023). While prior devices have been developed to monitor restenosis, most devices rely on pressure sensors to indirectly measure stenosis or blockage along an artery (Boutry et al., 2019; Chen et al., 2018; Ruth et al., 2021). In addition to possible inaccuracies in the correlation of pressure and stenosis depending on stenosis location and blood flow changes, tissue grows over endovascular sensors after implantation. This tissue growth inhibits the ability of the sensor to monitor pressure. Rather than monitor restenosis via pressure changes, an advantageous and more direct option is to use a strain sensor to detect changes in arterial wall strain and stiffness. The growth of tissue and build-up will mechanically stiffen the artery, influencing arterial wall strain. While a strain sensor will also become embedded in the arterial wall over time, the strain sensor can continue sensing the expansion and contraction of the artery as it does not rely on interfacing with blood flow. However, owing to strict requirements of size and sensitivity for implantation and monitoring of minuscule changes in arterial wall strain, there have been limited demonstrations of arterial wall strain sensing (Bingger et al., 2012; Ruh et al., 2016). While previous work highlighted the potential for restenosis monitoring with an implantable strain sensor, there remain obstacles to integrating a soft strain sensor within a vascular stent to enable reliable catheter deployment and to further miniaturize a strain sensor without sacrificing sensitivity (Herbert et al., 2022). Firstly, a strain sensor should be miniaturized to fit within a vascular stent to avoid possible complications with stent implantation. Secondly, sensor design and operating principle should be studied to enhance sensitivity while enabling a decrease in sensor size.

Here, we report the development of a biocompatible, miniaturized strain sensor for integration with a wireless stent to monitor restenosis. A capillary-based printing approach with a microneedle is optimized to enable high-resolution printing with polymer and metal inks to create a capacitive strain sensor. The low-profile strain sensor is laminated on the inner surface of a wireless vascular stent to enable wireless monitoring of arterial strain via inductive coupling. The low-profile sensor is shown to be compatible with conventional catheter deployment. To fabricate the miniaturized capacitive strain sensor, ink and printing parameters are studied to enable a fully printed sensor with narrow, conductive traces. Experimental and computational studies of the sensing mechanism and sensor design are performed to maximize sensitivity while minimizing sensor size. Finally, the integrated stent and sensor device is demonstrated in an artery model to detect arterial strain and restenosis progression.

2. Materials and methods

2.1. Printing of sensors

The capacitive strain sensors rely on a sliding mechanism to change the overlapping electrode area, therefore changing the capacitance when strain is applied. To create this sensor, multiple materials were printed to allow for proper electrical conductivity and insulation. First, a silicon wafer was spin coated with polymethyl methacrylate (PMMA; Kayakli Advanced Materials) at 3000 RPM for 30 s, then cured at 180 °C for 3 min. Poly(pyromellitic dianhydride-*co*-4,4′-oxydianiline) amic acid solution (12.8 wt, % 80% NMP, 20% aromatic hydrocarbon; SigmaAldrich) was diluted using 1-Methyl-2-pyrrolidinone (NMP, ≥ 99.0%) in a 5:1 wt ratio and stirred at 800 RPM for 1 h to lower viscosity and form a printable polyimide (PI) ink. A capillary- and microneedle-based system (Microplotter II; Sonoplot) was used to print sensors. To print the PI ink, a 60-μm diameter glass capillary was used (Video S1). A printing speed of 1 mm/s was set for the nozzle and a voltage of 11.7 V was applied to the piezoelectric plate at an auto-calibrated frequency. This ultrasonic signal vibrates the needle to create the meniscus needed to print. The microneedle was initially set to contact the substrate to form a meniscus, then raised by 10 μm without losing the meniscus to avoid collisions with surface imperfections. After printing, the PI layer was cured at 140 °C for 45 min. Two additional layers of PI were calibrated and printed on the initial layer using the same process. The printed PI was then plasma treated for 60 s using a handheld corona treater (Electro-Technic BD-20AC) to create a hydrophilic surface for successful ink adhesion. Silver (Ag) ink was prepared by mixing a silver nanoflake solution (HPS-FG32; Novacentrix) and Diethylene Glycol Butyl Ether (Butyl Carbitol ≥ 99%, Sigma Aldrich) in a 10:1 wt ratio. A 100 μm ceramic micropipette was filled with silver ink and printed on the treated PI surface (Video S2). A voltage of 2.3 V at an auto-calibrated frequency was applied to the piezoelectric plate to dispense ink. The Ag layers were printed at 1 mm/s before curing on a hotplate at 250 °C for 5 min. After completing the multi-layered printing of PI and Ag, the wafer was placed in an acetone bath for 1 h at 65 °C to remove the PMMA layer and release the printed sensors. Water soluble tape (AQUASOL) was used to peel off sensor plates, then dissolved in water to release the plate onto an elastomer film. A 5:1 mixture of polydimethylsiloxane (PDMS; Sylgard 184, Dow Corning) spin-coated at 1000 RPM and cured at 185 °C was used for sensor encapsulation. The sensor plates were stacked on top of each other while aligning the fingers with the PI edges extending in opposite directions. The PDMS films were laminated together with uncured PDMS and cured at 85 °C for 20 min.

2.2. Fabrication of a stent and integration with sensors

Stents were fabricated from a stainless-steel tube (304SS 14XX; Vita Needle Inc.) using a rotational stage and femtosecond laser (OPTEC). The stent was designed as an inductive coil with serpentine struts to allow for mechanical expansion and electrical conductivity as an antenna. The 4W laser was set to 62% power with 7 cut repetitions at a linear and rotational speed of 3.65 mm/s. After laser machining, the stent structure was sonicated in DI water to remove excess material. Stents were then electropolished using a stainless steel electropolish solution (E972; ESMA) for 1 min with a direct current of 0.5 A in order to clean the surface and prepare the surface for the electroplating of gold. Stents were sonicated in DI water to remove the electropolish solution before electroplating with an electroless gold plating solution (Sigma Aldrich) and Gamry three-electrode setup. The plating solution was maintained between 55 °C and 65 °C during 500 cycles. The stent was rotated every 100 cycles for uniform coating along the stent struts. The stents were coated in an approximately 15 μm layer of gold to reduce resistance of the stents from approximately 35 Ω–4 Ω. Lastly, the stents were insulated with a 5 μm, biocompatible layer of Parylene C (Laboter 3; Specialty Coating Systems). The printed sensors were inserted into the inner surface of the stent, with the exposed silver end of the sensor contacting the end of the stents. The sensor was electrically connected to the stent ends using quick-drying silver paint (Fast Drying Silver Paint; Ted Pella). These connections were coated with PDMS and cured with hot air at 180 °C to encapsulate (Fig. S1).

2.3. Sensor characterization

A motorized test stand (ESM303; Mark 10) was used to apply linear displacement and strain to sensors for optimization studies. Sensor

capacitance was measured with an LCR meter (BK891; B&K Precision) and recorded with a custom interface (LabView). The applied strain was controlled by setting a displacement to achieve a maximum strain of 5% for all characterization tests. The strain was calculated using the below equation:

$$\varepsilon = \frac{\Delta l}{l_0} \quad \text{(Eq. 1)}$$

The same setup was used for cyclic testing to characterize the lifetime of the sensors. Each sensor underwent 5% strain for 1000 cycles. Bending tests were also performed to evaluate the sensor strain durability with the sensor rotated 90°, to simulate potential bends a stent may experience during deployment in narrow arteries.

2.4. Mathematical models

A computational model was developed to evaluate the impact of sensor finger geometry on strain sensitivity. The model estimates the change in the area of the capacitive sensor, dependent upon the alignment of the overlapping fingers. Sensor geometries were created in a CAD program (Rhinoceros 3D, Robert McNeel, and Associates) and converted to point clouds representing the outer boundary of the sensor fingers. Point clouds were imported to Matlab, and a custom code analyzed the overlapping area of two sensor fingers while displacements were applied. The model assumes the separation distance of the two plates, and the dielectric constant does not change with strain. Additionally, the model does not account for sensitivity changes resulting from elastomer stretching and slipping between PI and elastomer. However, the model provides insight into the importance of sensor finger geometry on sensitivity.

2.5. Restenosis testing

Integrated stents and sensors were expanded using a 4 mm diameter balloon catheter. The device was then implanted into a silicone (Ecoflex 30, Smooth-On) artery model with a 3.8 mm inner diameter. The device was embedded in the silicone arterial wall, mimicking the expected tissue growth over an implanted stent. The mock artery used a wall thickness of 2 mm, which was previously shown to provide a biomimetic performance of a coronary artery (Elsisy et al., 2021).

To include the progression of restenosis, or a narrowing of the artery, a mold was created to represent 60% and 75% occlusion. The mold was inserted into the silicone arterial model and filled with silicone. After curing for 2 h, a narrower section inside the modeled artery was created. The 60% and 75% occlusions were sequentially tested for each artery. A pulsatile flow pump (Series 1400, Harvard Apparatus) controlled fluid flow at a stroke volume of 1.5 mL with 60 strokes per minute. The arterial strain was optically measured by recording videos and analyzing artery diameter in a frame-by-frame manner (Video S3). Frames of videos were converted to black and white images to track the location of the edges of the white artery against a black background. Wired testing was performed on implanted sensors to ensure sensor capacitance correlated with arterial strain. The capacitance of the sensor was measured with the use of an LCR meter while pressure was monitored using a commercial sensor (Honeywell 26PCBFB6G) and its voltage was measured by a digital multimeter (Model 2100, Keithley). Wireless testing was performed using a vector network analyzer (VNA; TTR506A; Tektronix) connected to an external loop antenna inductively coupled with the device (Fig. S2). The S_{11} parameter of the network was monitored with continuous frequency sweeps to locate the resonant frequency of the stent-sensor system. At the resonance frequency, a sharp drop on the S_{11} parameter can be observed due to the increase in the power transfer efficiency. The pressure was monitored the same way as the wired testing.

2.6. Toxicity biocompatibility study

To assess in vitro biocompatibility of the printed strain sensor devices, cytotoxicity to vascular smooth muscle cells (VSMCs) was investigated using both CCK-8 assay (Enzo Life Sciences, USA) and live/dead staining assay (Invitrogen, USA). For elution testing, 0.05 g of the printed sensor, PDMS, and ePTFE samples (0.1 g/mL) were incubated in 500 μL of cell culture medium at 37 °C. Then, the extracted solutions from each sample were collected after 24 h. For cell viability testing, the VSMCs were seeded onto 96-well plates (1 × 104 cells/well) and incubated for 6 h under standard culture conditions (37 °C and 5% CO2) to allow for cell adhesion. Then, the adhered cells were treated with each extracted solution (24 h) and incubated for another 24 h. As a control, the fresh medium without sample incubation was used. After 24 h, the CCK-8 assay reagents were added to each well, and the plates were incubated for 2 h at 37 °C. The optical density (O.D.) was measured at 450 nm using a microplate reader (GloMax Discover, Promega, USA) to quantify the dehydrogenase activity of the viable cells. The experiments were performed in triplicate. Morphological change and cell viability of VSMCs cultured with each extracted solution were also observed using an ECHO Revolve microscope (BICO company, USA) in fluorescent mode. For live/dead staining assay, the cultured cells with extracts were incubated for 30 min in a mixture solution containing both calcein AM and ethidium homodimer-1 (Invitrogen, USA) and then were imaged.

3. Results and discussion

3.1. Overview of a soft implantable bioelectronic system

This work introduces a printed, miniaturized bioelectronic system with soft strain sensors for wireless restenosis monitoring. The illustration in Fig. 1A captures the overview of the sensor-integrated system, implanted in a blood vessel. The operating principle of this device relies on an LC circuit, which is created by the electrical connection of an inductive stent and a capacitive sensor, as seen in Fig. 1B. In an LC circuit, the resonant frequency changes with shifts in capacitance, which is proportional to the strain the artery undergoes (Huang et al., 2016). This allows the device to detect tissue build-ups over months or years occurring within the stent (Fig. 1C). For example, the bioelectronic system can wirelessly detect arterial strain signals captured over time to identify the progression of restenosis (Fig. 1D). Photos in Fig. 1E and F shows fabricated devices, including a wireless stent and thin-film miniaturized strain sensor. We used a microneedle capillary system to print these sensors (Fig. 1G), which are highly flexible and low profile (Fig. 1H). Those sensors are easily and seamlessly integrated with the fabricated stent inside (Fig. 1I), which can be deployed by a balloon catheter and a guide wire (Fig. 1J).

3.2. Fabrication of sensors and stents

Our printing system used tuned PI and Ag inks to print thin-film strain sensors (Fig. 1B). As illustrated in Fig. 2A, the microneedle fills with ink and uses a piezoelectric plate to create an ultrasonic vibration and form a meniscus to dispense ink, which allows for high-resolution of printing. Here, we apply this printing method to enable high-resolution printing of strain sensor fingers. Previous work noted the relation of finger width to sensitivity, but the printed sensor used feature sizes of 300 μm (Herbert et al., 2022). Additionally, miniaturizing sensor features are critical to integrating a strain sensor on the inner surface of a narrow (<2 mm diameter) vascular stent. Compared to other printing methods, including aerosol jet, screen, and inkjet printing, the capillary-based system, used in this work, offers high-resolution printing with an ink viscosity range acceptable for printing polymer and metal inks (Table S1). Fig. 2B shows an image of high-resolution printing with PI ink and an enlarged view of calibrated printing on top of a previously printed Ag layer. Using this printing system, multi-layered printing was

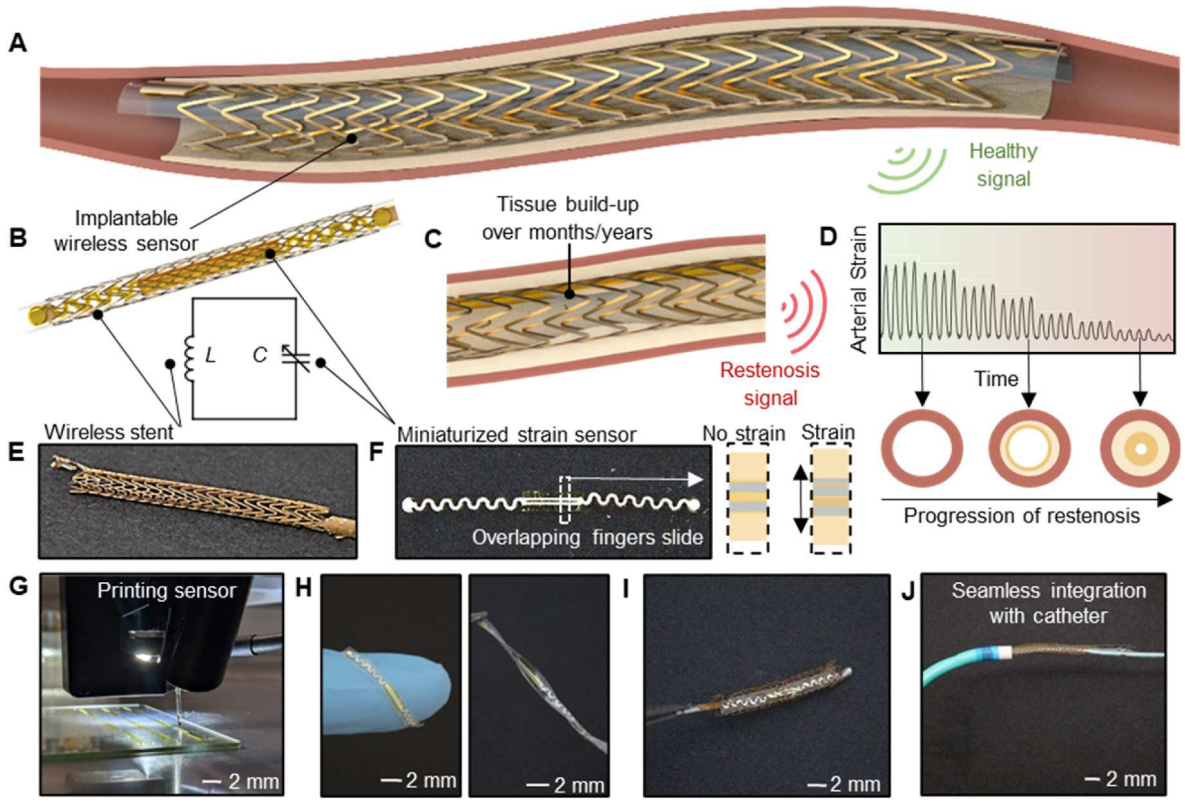

Fig. 1. Overview of a soft implantable bioelectronic system for wireless restenosis monitoring. (A) Illustration of the wireless vascular device implanted in an artery. (B) Diagram of the implantable device consisting of a wireless stent and capacitive strain sensor with correlating LC circuit (C) Depiction of restenosis occurring within the implanted stent. (D) Simulated wireless signals captured over time to identify the progression of restenosis. (E) Photo of the wireless stent. (F) Photo of miniaturized strain sensor highlighting the effects of strain in finger alignment. (G) Image of printing needle used to fabricate strain sensors. (H) Photos of a printed strain sensor on a finger (left) and twisted by tweezers (right). (I) Integrated stent and sensor. (J) The miniaturized strain sensor attached to the stent inside enables reliable deployment with a guide and balloon catheter.

performed to create the sensor layers illustrated in Fig. 2C. The sensor design consists of two sliding plates of printed PI and Ag (Fig. 1F). Each plate contains Ag fingers responsible for the change in capacitance when strain is applied. Each set of fingers is attached to a serpentine interconnect leading to circular pads on opposite sides for connection to a wireless inductive stent, forming the resonant circuit. Since the viscosity of PI is too high to be printed with a microneedle, its precursor, polyamic acid, was dissolved with NMP to lower the viscosity, similar to what has been reported for inkjet printing (Zhang et al., 2016). Different solvent concentrations were tested until the 60 μm-diameter glass microneedle could load and dispense PI ink without leakage reliably. As a result of the high viscosity of the ink, a slow print speed was coupled with a high potential to dispense PI consistently. A single layer of PI was measured to have a thickness of around 3 μm. Sensors with up to three layers of PI were characterized, as shown in Fig. 2D. Due to the thin deposition of the diluted PI ink, sensors with one and two layers proved to be too fragile. These sensors could not successfully transfer to the elastomer layer for assembly (Fig. S3A, Video S4). Three layers of PI allowed successful transfer from the glass slide to the elastomer for sensor encapsulation and were used before printing Ag layers onto the printed PI (Fig. S3B, Video S5). Previous work has also proven that at least 10 μm are needed for successfully transferring printed PI (Kwon et al., 2020).

In addition to PI ink, the printing of Ag was evaluated to achieve consistent and high-resolution printing. The concentration of the Ag ink, which was adjusted by varying the ratio of solvent to ink, was studied to find the ideal viscosity in which the ink maintains a narrow line after printing. However, the ink must also be able to flow into and out of the microneedle. The second parameter to be tuned was printing speed, as higher printing speeds reduce process time and produce thinner lines but cause undesirable ink accumulation when the microneedle pauses. In addition, the potential of the ultrasonic signal was adjusted to enable uniform dispensing of Ag. To allow for the silver ink to be printed on top of PI, a corona treater was used to increase the wettability of the printed PI layers. Based on the optimized ink and settings (Table 1), the highest resolution print obtainable with the Ag ink was a 26 μm-wide trace, as shown in Fig. 2E (Fig. S4). However, this resolution was inconsistent, as it resulted in spreading at the ends of printed lines. Lines with widths less than 100 μm could be consistently achieved without spreading on glass substrates (Figs. S5 and S6), which was achievable with a 10 μm-diameter glass capillary. This small diameter capillary, however, was incompatible with printing on top of the printed PI surfaces due to the small variations in surface height and roughness.

Therefore, a 100 μm-diameter ceramic microneedle was selected for the Ag printing of sensors onto printed PI layers. A feature size of 200 μm was repeatedly printed with consistent width and aspect ratio throughout printing sessions, as shown in Fig. 2F. This consistency is critical for the strain sensor to provide a linear response at high sensitivity. A serpentine interconnected was printed to allow for stretchability and increase the robustness of the sensor to strain in the direction parallel to the artery, as illustrated in Fig. 2G. Fig. 2H summarizes the printing and assembly procedure of the strain sensor, which completes by encapsulating the sensor in the elastomer. The elastomer encapsulation insulates the capacitive sensor while maintaining a stretchable structure. The final assembled sensor is highly flexible, as demonstrated in Fig. 2I, enabling it to survive expanding within a stent and implanting inside the body. The soft, printed sensors were integrated with a wireless vascular stent fabricated via rotational laser machining (Fig. 2J). Here,

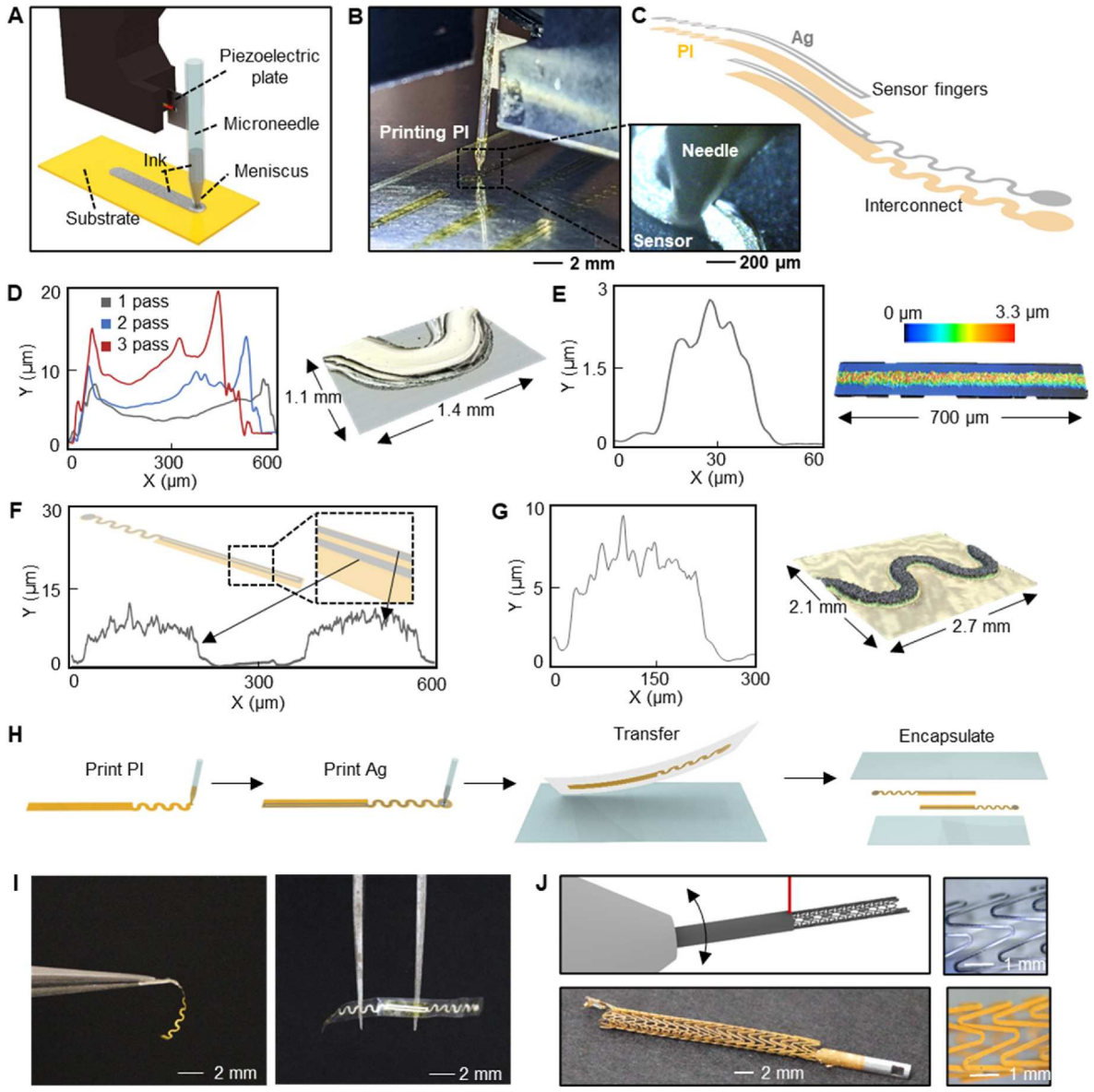

Fig. 2. Sensor printing using the microplotting technique. (A) Illustration and (B) photo of printing method using a microneedle driven by a piezoelectric element. The enlarged view of the needle shows the deposition of ink. (C) Exploded view of capacitive strain design using overlapping PI and Ag plates. (D) Cross-section profiles and 3D images of printed PI after multiple passes. (E) Profile of high-resolution, printed Ag trace with colored height scale. (F) Cross-section profile of printed Ag for sensor fingers. (G) Printed stretchable serpentine trace of PI and Ag. (H) Overall fabrication procedure for capacitive strain. (I) Photos of printed sensor plate (left) and assembled sensor (right). (J) Fabrication of stainless steel wireless stent (top) and electroplated gold stent (bottom).

Table 1
Ink and printing parameters for strain sensors.

	PI	Ag
Ink Solvent	NMP	Butyl Carbitol
Capillary Diameter (μ m)	60	100
Printing Speed (μ m/s)	1000	1000
Dispensing Potential (V)	11.7	2.3
Curing/sintering Temperature (°C)	140	250

we enhanced the laser machining of the wireless vascular stent by further optimizing fabrication parameters to enable smoother stent surfaces. These smoother surfaces, coupled with an extended period of electropolishing for 1 min, enabled stronger adhesion of electroplated gold to the stent compared to prior versions. Resistance of the stent was reliably lowered under 5 Ω to offer a wireless sensor with a high-quality factor (Fig. S7).

3.3. Optimization of strain sensor design

As explained above, the strain sensors consist of two plates that slide opposite each other when applying strain (Fig. 1F). When the fingers from both plates are aligned at 0% strain, the capacitance is at a maximum. As the sensor is strained, the plates slide, and thus capacitance decreases, as illustrated in Fig. 3A. To incorporate the sensor within the stent, the sensor was restricted to a width smaller than the 2.1 mm diameter of the unexpanded vascular stent. The key design parameters were explored to optimize the balance between miniaturization and high sensitivity, including finger geometry and extended support plates (Fig. 3B and C). The sliding mechanism relies on the overlapping plates to be displaced in opposite directions. This motion stems from the asymmetrical extension of PI for the sensor plates. Based on this, strain sensitivity was evaluated for sensors using different plate extension lengths. Linear strains were applied using a mechanical stretcher for optimization studies (Fig. S8). A maximum of 5% strain was

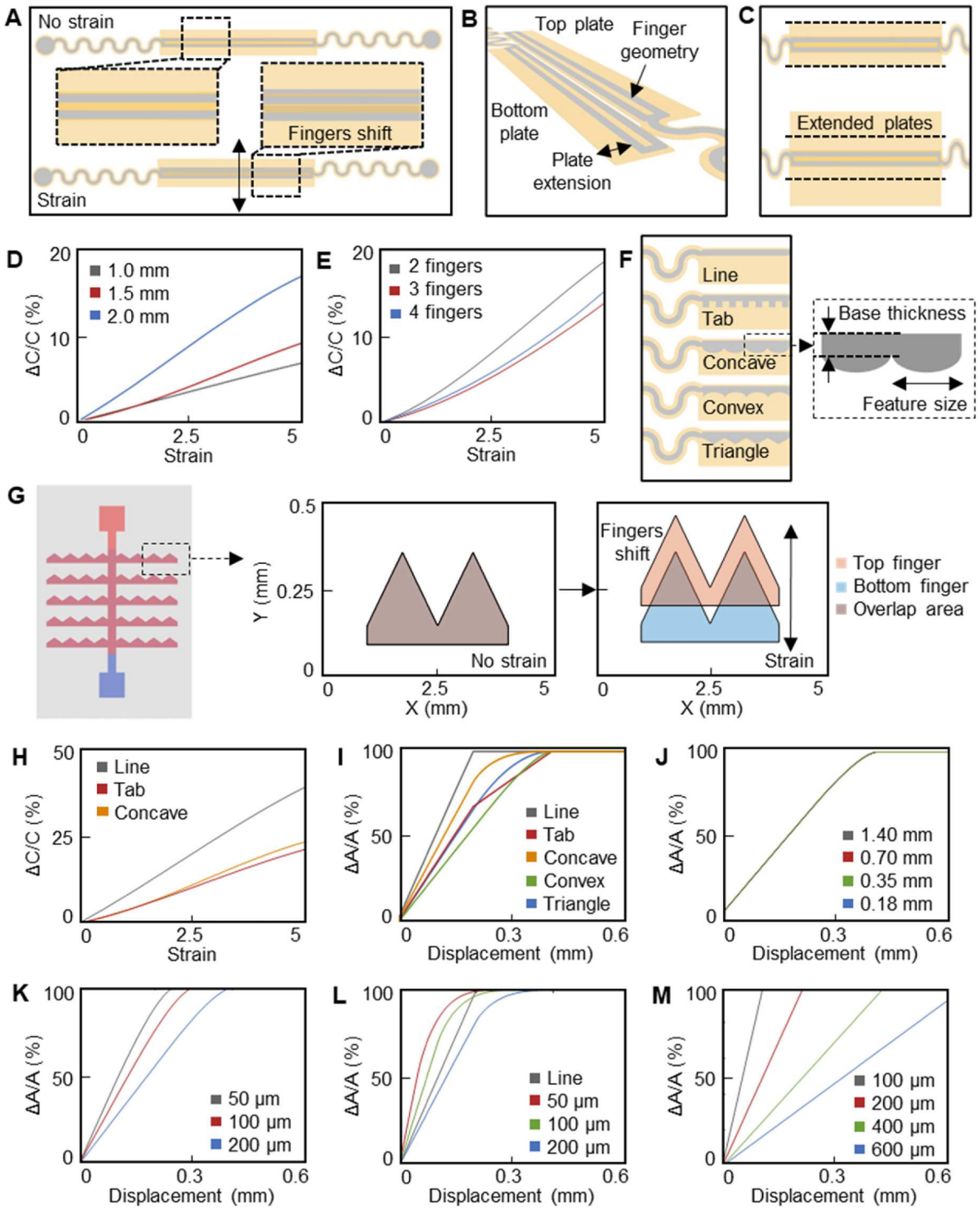

Fig. 3. Optimization of miniaturized strain sensor for high sensitivity. (A) Illustration of sensing mechanism for capacitive strain sensor. (B–C) Features, including finger geometry and polymer extensions, that impact sensitivity. (D–E) Strain sensitivity for sensors with (D) different lengths of polymer extensions and (E) number of fingers. Longer polymer extensions improve sensitivity by enabling stronger coupling of finger movement with applied strain. (F) Illustration of finger shapes and parameters studied. (G) Computational model of strain sensor sensitivity used to evaluate different geometries by simulating the overlapping area of the capacitor. (H) Experimental results of sensitivity for different finger shapes. (I) Comparison of sensitivities for different finger shapes from a computational model. (J–M) Computational model results for (J) different feature sizes of finger structures, (K) base thickness of finger structures, (L) convex finger structures with different base thicknesses, and (M) straight lines of different thicknesses. Notably, a convex finger structure with a thin base thickness outperforms a straight finger line.

applied for all tests, which encompasses the range of expected arterial strains (Back et al., 1994; Nakatani et al., 1995; Numao et al., 1997). As shown in Fig. 3D, sensors with different extension lengths of 1.0 mm, 1.5 mm, and 2.0 mm were evaluated. A longer plate was found to improve sensitivity. Sensors with a 0.5 plate length were also characterized, but were incapable of detecting strain. While sensitivity increases with extension, the inner diameter of the stent limits the size of the integrated sensor. Sensitivity was similarly found to scale with the ratio between finger width and extension width. Thus, printing a narrower sensor finger and decreasing the overall sensor length without

losing sensitivity is possible. All tested sensors used a ratio of 1:1 for finger width and plate extension. In addition, the number of fingers was varied to determine the minimum number of fingers for the strain sensor. Sensors with one to four fingers were evaluated, but sensors with one finger were inconsistent in strain detection. As shown in Fig. 3E, the number of fingers plays a minor role in determining sensitivity, which agrees with previous findings (Herbert et al., 2022). Based on this, sensors integrated with the stent used two fingers to minimize sensor size.

In addition, while straight-line fingers are commonly used for both interdigitated and sliding capacitive strain sensors, the geometry of the fingers was evaluated. Fig. 3F illustrates the finger shapes studied here, along with parameters of feature size and base thickness. Alternate sensors were created, as shown in Fig. 3G, to study the effects of finger shape on sensor sensitivity. They operate under the same sliding mechanism as the original sensor design using straight line fingers and were used to understand if the change in overlapping area could be increased per an applied strain. We have also included more arrows and detailed labels in Fig. 3F to better demonstrate the sliding mechanism of the sensor. Fig. 3H shows experimental results comparing sensors using fingers of straight lines, tabs, and concave domes. Here, straight lines are observed to offer the highest sensitivity. To validate this finding, a mathematical model was created to calculate the overlapping area of fingers during strain. Fig. 3I summarizes the results from the model with additional finger shapes. Overall, the mathematical model agrees with the experimental results. A validated computational model was applied to provide further insight into the importance of finger shapes for sliding strain sensors (Fig. S9). Fig. 3J shows feature size of concave domes has no impact on sensitivity. Fig. 3K explores the relationship between base thickness and sensitivity, and indicates that a thinner base improves

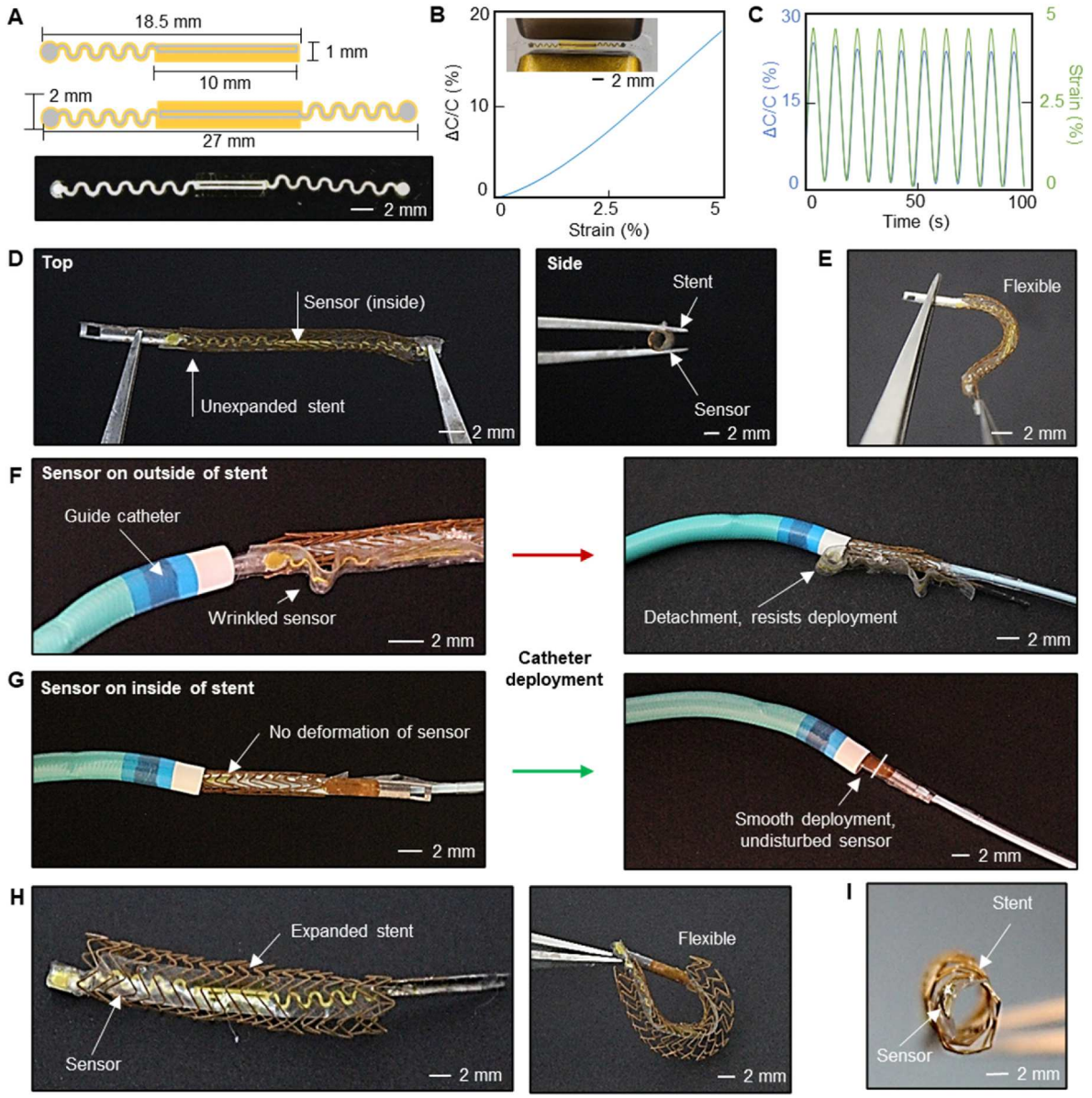

Fig. 4. Characterization of restenosis sensor and integration with a stent for catheter deployment. (A) Illustration and photo of a miniaturized sensor for integration inside of the stent. (B) Sensor capacitance change with applied linear strain. (C) Cyclic testing of sensor capacitance. (D) Top and side images of the integrated stent and sensor with low profile cross-section. (E) Image demonstrating the high flexibility of the integrated device. (F) Images showing catheter deployment of a device with a sensor attached to the outer surface. The sensor detaches due to shear forces from the catheter. (G) Attaching the sensor on the inside of the stent enables the device to fit into a guide catheter for deployment. (H) Photos of the device after stent expansion with a balloon catheter. (I) Cross-section image of expanded stent and sensor showing a low-profile form of sensor.

sensitivity. This derives from lowering the initial overlapping area to realize a greater percent change in the overlapping area. Using this knowledge, convex features were simulated using different base thicknesses. Fig. 3L shows that a convex structured finger can outperform a straight line with a thin base. Similar to the effect of base thickness, the model verifies that straight-line fingers can offer improved sensitivity by decreasing line width (Fig. 3M). The thinner the lines are, the more sensitive the sensors are for detecting strain. With the microneedle printing system, the average line thickness was 200 μm, but future studies will be explored to enable higher sensitivity sensors.

3.4. Stent and sensor integration and deployment

After optimization, the final sensors used for integration with a stent consisted of two fingers with a 1:1 ratio of finger geometry width to PI extended plates. Fig. 4A shows a printed sensor and relevant geometry. This resulted in an average capacitance change of 18%, with a maximum capacitance change of 26%, at 5% strain, as shown in Fig. 4B and C. In prior work, sliding capacitive sensors presented less than a 10% change in capacitance at 5% strain, which shows the increased sensitivity in the presented work (Herbert et al., 2022). There are not many studies utilizing a sliding strain sensor, however one other design displayed a 50% change in capacitance for 15% strain (Boutry et al., 2018). Assuming a linear relationship, it translates to a 17% change for 5% strain, which is a lower sensitivity than what was seen in this study. In addition, this sensor is significantly larger than the one designed for artery implantation, which highlights the strides made in the sensitivity of these sensors (Table S2). The sensors also displayed stable performance throughout 1000 cycles of strains above 5%, which is the maximum expected arterial wall strain (Fig. S10) (Back et al., 1994; Nakatani et al., 1995; Numao et al., 1997). When comparing the first 5 cycles with the last 5 cycles of the test, the base capacitance dropped by 1.1%, while the sensitivity dropped by 4.1%. This is the same as when it undergoes 500 cycles of cyclic bending (Fig. S11). After the 500 cycles, a 4.9% drop in base capacitance was observed.

After sensor optimization led to a decrease in sensor width to 2 mm, the sensor was threaded through an unexpanded stent to ensure its integration on the inner surface of the stent. This low-profile integration can be seen in Fig. 4D. The thin, printed layers of the sensor allowed for flexibility with the stent as well, without breaking the serpentine connections and maintaining its connection electrically to the stent, as seen in Fig. 4E. Owing to the low-profile form of the sensor, the sensor placement did not obstruct loading the integrated stent and sensor device onto a balloon catheter. It was expected that integrating the sensor within the stent would be a more clinically promising design than the previously shown sensor attachment to the outer surface of the stent (Herbert et al., 2022). This was validated by inserting the stent and sensor device through the tip of a guide catheter (Cordis, 8F). First, the sensor with the stent attached to the outside was loaded onto a balloon catheter and pushed through the guide catheter. As shown in Fig. 4F, the sensor easily wrinkles on the stent when contacting the catheter and, if pushed further, detaches and obstructs deployment. This was followed with two additional devices, where the same results were observed (Fig. S12). Fig. 4G demonstrates the same catheter insertion process with the miniaturized sensor integrated into the inner surface of the stent. As seen in the images, the stent easily slides into the catheter, without inducing shear stress in the sensor, reducing the sensor failure and complication risk during the deployment process (additional visual in Fig. S13). Two additional devices were inserted into an 8F, then a smaller, 7F catheter with successful deployment in all three. Following guidance through the guide catheter, the integrated stent and sensor were expanded using a balloon catheter (Fig. S14). Fig. 4H displays the expanded stent and sensor and the high degree of flexibility offered. After expansion, the sensor must maintain a low profile to avoid any flow obstruction within an artery. As shown in Fig. 4I, the sensor lays flat against the stent and does not show a visual indication of flow blockage.

3.5. In vitro restenosis detection

Based on printing optimization and sensor characterization, the strain sensor was designed to detect minuscule changes in arterial stiffness caused by restenosis. As shown in Fig. 5A, the arterial model was used to evaluate sensor signals during the progression of restenosis. The strain sensor is expected to observe less strain as restenosis increases and locally stiffens the artery. Despite embedding the stent and sensor into the silicone artery, the model artery maintains high flexibility, as shown in Fig. 5B. To simulate blood flow, the pulsatile flow was controlled through the artery model with wireless sensing (Fig. S15). During wired testing and recording of sensor capacitance, arterial pressure was monitored simultaneously with arterial strain, as seen in Fig. 5C–H. We recorded videos to measure strain optically (Fig. S16). Fig. 5C–E shows a slow, steady increase in pressure leads to a similar increase in arterial strain. This increase in strain causes an identical decrease in sensor capacitance. Fig. 5F–H shows a similar relationship at a faster pressure pulse rate (additional details in Fig. S17). The strain sensor can also detect varying shifts in flow rate, as seen in Fig. 5I (additional details in Fig. S18). With real-time monitoring, the sensor can detect pulse rate, or heart rate, in addition to arterial strain. The arterial model also validated wireless sensing of arterial strain and restenosis progression during pulsatile flow (Fig. S19). Fig. 5J displays a set of frequency sweeps used to identify resonance, where resonance increase with arterial strain (additional visual in Fig. S20). Fig. 5K displays results from real-time, wireless monitoring of arterial strain at different restenosis levels. At 0% restenosis, a 2.5% change in resonant frequency was detected wirelessly. This magnitude decreases as restenosis increases, with 75% restenosis leading to less than 1% resonant frequency change for the same heart rate and stroke volume. Wireless results are summarized in Fig. 5L, showing the correlation between resonant frequency change and restenosis. Compared to previous designs, there is a larger change in resonance detected, with an approximately 3-times increase in wireless sensitivity compared to prior work, which derives from the miniaturized sensor (Herbert et al., 2022). This higher sensitivity may potentially detect smaller changes in restenosis progression and, clinically, may enable more proactive treatment of patients (Cassese et al., 2015; Joner et al., 2006; Omeh and Shlofmitz, 2023). In future studies, smaller increases in restenosis will be studied to explore the sensing limitations of the printed strain sensor.

3.6. In vitro cytotoxicity evaluation

The materials chosen for the stent and the sensor have been tested in previous works and proven to show both biocompatibility and hemocompatibility. The stent is coated in 5 μm of parylene, a biocompatible material (Kuo et al., 2021). The sensors are fully encapsulated in PDMS, the sole material interacting with the body. In addition to selecting these known compatible materials, the sensor was tested in a 24-h cytotoxicity study. Cells have remained viable when tested with a fully encapsulated sensor (Fig. S21). The viability of the cells with the sensor is comparable to PDMS without a sensor, as well as to ePTFE, an FDA-approved biocompatible material.

4. Conclusion

This paper reports on a fully printed strain sensor designed for unobtrusive integration with a wireless vascular stent to monitor in-stent restenosis wirelessly. For the first time, the printing of widely used PI is demonstrated using a microneedle-based printing system. By tuning ink and printing parameters, a miniaturized yet highly sensitive capacitive strain sensor is developed for attachment along the inner surface of a stent. This sensor placement improves device compatibility with conventional catheterization procedures. The sensor design is also studied, providing further insight into routes to enhance sensitivity at an increasingly compact size. The printed sensor enables the detection of

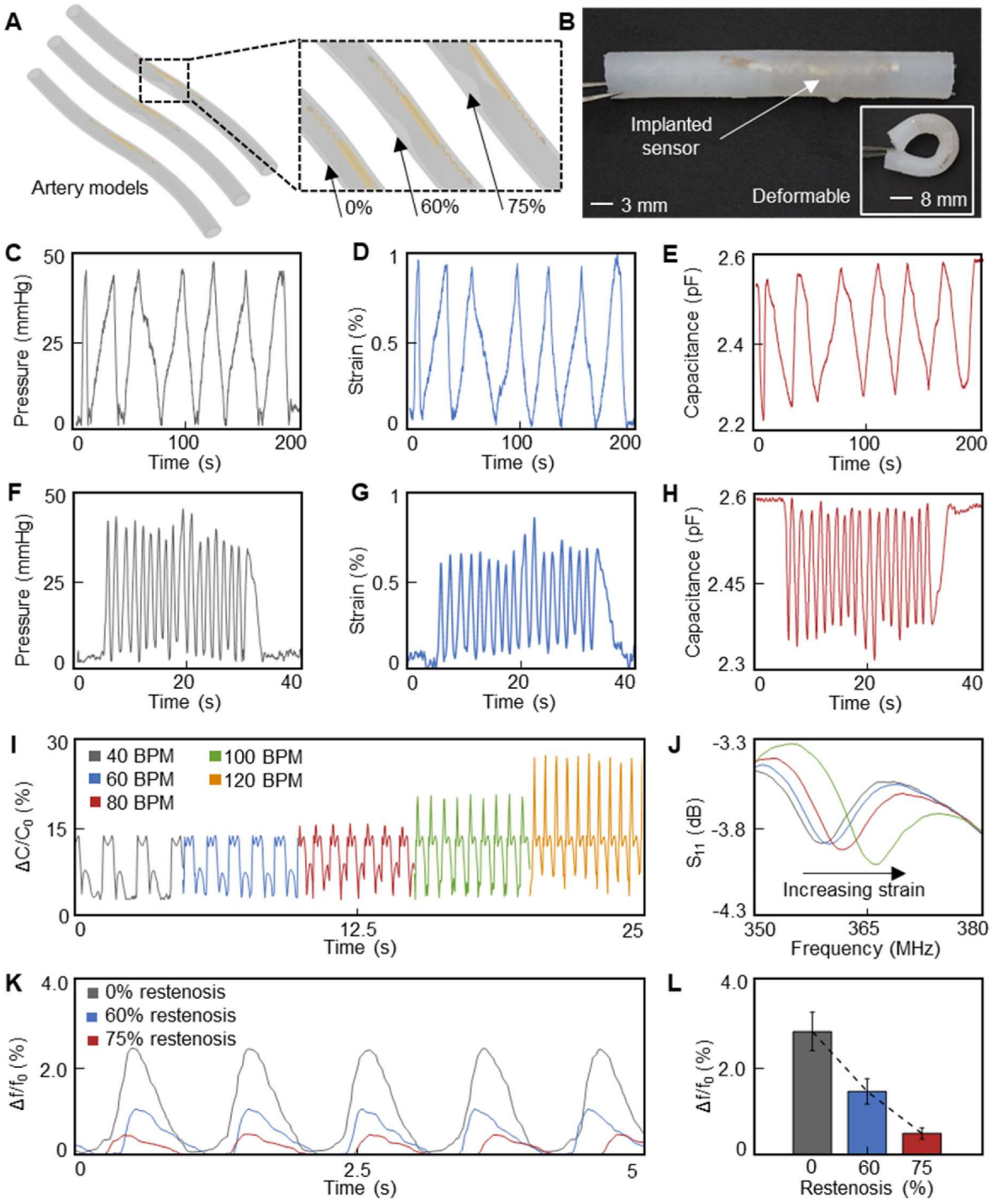

Fig. 5. Sensing of arterial strain and restenosis progress. (A) Illustration of artery models used to test the progression of restenosis. (B) Photo of wireless stent and sensor implanted in artery model. (C–E) Pressure, arterial strain, and sensor capacitance during applied pressure changes. Pressure changes control arterial strain, which the sensor captures. (F–H) Pulsatile changes in (F) pressure and (G) arterial strain compare well with (H) sensor capacitance. (I) Sensor capacitance during pulsatile flow at different pulse rates. (J) Wireless signal acquired from stent and sensor in artery model. Resonant frequency increases as strain increases. (K) Comparison of wirelessly measured resonant frequency changes at different restenosis levels. (L) Summary of resonance changes at 3 stages of restenosis, indicating the device's ability to monitor restenosis.

arterial strain with high sensitivity. Further studies should focus on the optimization of wireless performance to enhance reading distance. Additionally, in vivo trials may be performed to test sensor performance and further validate the improvements made to sensor size and sensor integration with a stent. This work demonstrates an improved strain sensor that can be used in various applications, including characterizing vascular flow and heart volume, where minuscule strain changes need to be detected. Collectively, the developed printing method offers an opportunity for high-resolution printing of other implantable biosensors and their miniaturization.

CRediT authorship contribution statement

Bruno Rigo: Conceptualization and formal analysis, Writing –

original draft.

Allison Bateman: Conceptualization and formal analysis, Writing – original draft.

Jimin Lee: Data curation.

Hyeonseok Kim: Data curation.

Yunki Lee: Data curation.

Lissette Romero: Data curation.

Young C. Jang: Data curation, Resources, Supervision.

Robert Herbert: Conceptualization and formal analysis, Writing – original draft.

Woon-Hong Yeo: Conceptualization, Funding acquisition, Project administration, Resources, Supervision, Writing – review & editing.

Declaration of competing interest

The authors declare the following financial interests/personal relationships which may be considered as potential competing interests: Georgia Tech has a pending US patent application.

Data availability

Data will be made available on request.

Acknowledgements

We acknowledge the support of the National Institutes of Health (NIH R03EB028928). This study was partially supported by the IMat-IBB Materials for Biomedical Systems Initiative and the IEN CHCIE Grant from the Georgia Tech Institute for Electronics and Nanotechnology. This work was also supported by the Georgia Tech IEN Center for Human-Centric Interfaces and Engineering. Electronic devices in this work were fabricated at the Institute for Electronics and Nanotechnology, a member of the National Nanotechnology Coordinated Infrastructure, which is supported by the NSF (grant ECCS-2025462).

Appendix A. Supplementary data

Supplementary data to this article can be found online at https://doi.org/10.1016/j.bios.2023.115650.

References

Alfonso, F., Byrne, R.A., Rivero, F., Kastrati, A., 2014. Current treatment of in-stent restenosis. J. Am. Coll. Cardiol. 63, 2659–2673. https://doi.org/10.1016/j.jacc.2014.02.545.

Atherosclerosis, 2022a [WWW Document]. Treatment | NHLBI, NIH. URL. https://www.nhlbi.nih.gov/health/atherosclerosis/treatment, 2.19.23.

Atherosclerosis, 2022b [WWW Document]. What is atherosclerosis? | NHLBI, NIH. URL. https://www.nhlbi.nih.gov/health/atherosclerosis, 2.19.23.

Back, M., Kopchok, G., Mueller, M., Cavaye, D., Donayre, C., White, R.A., From the Department of Surgery, H.-U.M.C., Torrance, 1994. Changes in arterial wall compliance after endovascular stenting. J. Vasc. Surg. 19, 905–911. https://doi.org/10.1016/S0741-5214(94)70017-6.

Bingger, P., Zens, M., Woias, P., 2012. Highly flexible capacitive strain gauge for continuous long-term blood pressure monitoring. Biomed. Microdevices 14, 573–581. https://doi.org/10.1007/s10544-012-9636-9.

Boutry, C.M., Beker, L., Kaizawa, Y., Vassos, C., Tran, H., Hinckley, A.C., Pfattner, R., Niu, S., Li, J., Claverie, J., Wang, Z., Chang, J., Fox, P.M., Bao, Z., 2019. Biodegradable and flexible arterial-pulse sensor for the wireless monitoring of blood flow. Nat. Biomed. Eng. 3, 47–57. https://doi.org/10.1038/s41551-018-0336-5.

Boutry, C.M., Kaizawa, Y., Schroeder, B.C., Chortos, A., Legrand, A., Wang, Z., Chang, J., Fox, P., Bao, Z., 2018. A stretchable and biodegradable strain and pressure sensor for orthopaedic application. Nat Electron 1, 314–321. https://doi.org/10.1038/s41928-018-0071-7.

Cassese, S., Byrne, R.A., Schulz, S., Hoppman, P., Kreutzer, J., Feuchtenberger, A., Ibrahim, T., Ott, I., Fusaro, M., Schunkert, H., Laugwitz, K.-L., Kastrati, A., 2015. Prognostic role of restenosis in 10 004 patients undergoing routine control angiography after coronary stenting. Eur. Heart J. 36, 94–99. https://doi.org/10.1093/eurheartj/ehu383.

Chen, X., Assadsangabi, B., Hsiang, Y., Takahata, K., 2018. Enabling angioplasty-ready "smart" stents to detect in-stent restenosis and occlusion. Adv. Sci. 5, 1700560 https://doi.org/10.1002/advs.201700560.

Cheng, G., Chang, F., Wang, Y., You, P.-H., Chen, H., Han, W., Wang, J., Zhong, N., Min, Z., 2019. Factors influencing stent restenosis after percutaneous coronary intervention in patients with coronary heart disease: a clinical trial based on 1-year follow-up. Med. Sci. Mon. Int. Med. J. Exp. Clin. Res. 25, 240–247. https://doi.org/10.12659/MSM.908692.

Elsisy, M., Herbert, R., Yeo, W.-H., Pacella, J.J., Chun, Y., 2021. Development of a nanosensor-integrated stent for wireless, continuous monitoring of restenosis progression. In: Nano-, Bio-, Info-Tech Sensors and Wearable Systems. Presented at the Nano-, Bio-, Info-Tech Sensors and Wearable Systems. SPIE, pp. 15–25. https://doi.org/10.1117/12.2582378.

Herbert, R., Elsisy, M., Rigo, B., Lim, H.-R., Kim, H., Choi, C., Kim, S., Ye, S.-H., Wagner, W.R., Chun, Y., Yeo, W.-H., 2022. Fully implantable batteryless soft platforms with printed nanomaterial-based arterial stiffness sensors for wireless continuous monitoring of restenosis in real time. Nano Today 46, 101557. https://doi.org/10.1016/j.nantod.2022.101557.

Huang, Q.-A., Dong, L., Wang, L.-F., 2016. LC passive wireless sensors toward a wireless sensing platform: status, prospects, and challenges. J. Microelectromech. Syst. 25, 822–841. https://doi.org/10.1109/JMEMS.2016.2602298.

Joner, M., Finn, A.V., Farb, A., Mont, E.K., Kolodgie, F.D., Ladich, E., Kutys, R., Skorija, K., Gold, H.K., Virmani, R., 2006. Pathology of drug-eluting stents in humans. Delayed healing and late thrombotic risk. J. Am. Coll. Cardiol. 48, 193–202. https://doi.org/10.1016/j.jacc.2006.03.042.

Kastrati, A., Mehilli, J., Dirschinger, J., Pache, J., Ulm, K., Schühlen, H., Seyfarth, M., Schmitt, C., Blasini, R., Neumann, F.J., Schömig, A., 2001. Restenosis after coronary placement of various stent types. Am. J. Cardiol. 87, 34–39. https://doi.org/10.1016/s0002-9149(00)01268-6.

Kuo, W.-C., Wu, T.-C., Wu, C.-F., Wang, W.-C., 2021. Bioperformance analysis of parylene C coating for implanted nickel titanium alloy. Mater. Today Commun. 27, 102306 https://doi.org/10.1016/j.mtcomm.2021.102306.

Kwon, Y.-T., Kim, Y.-S., Kwon, S., Mahmood, M., Lim, H.-R., Park, S.-W., Kang, S.-O., Choi, J.J., Herbert, R., Jang, Y.C., Choa, Y.-H., Yeo, W.-H., 2020. All-printed nanomembrane wireless bioelectronics using a biocompatible solderable graphene for multimodal human-machine interfaces. Nat. Commun. 11, 3450. https://doi.org/10.1038/s41467-020-17288-0.

Nakatani, S., Yamagishi, M., Tamai, J., Goto, Y., Umeno, T., Kawaguchi, A., Yutani, C., Miyatake, K., 1995. Assessment of coronary artery distensibility by intravascular ultrasound: application of simultaneous measurements of luminal area and pressure. Circulation 91, 2904–2910. https://doi.org/10.1161/01.CIR.91.12.2904.

Numao, T., Ogawa, K., Fujinuma, H., Furuya, N., 1997. Pulsatile diameter change of coronary artery lumen estimated by intravascular ultrasound. J. Cardiol. 30, 1–8.

Omeh, D.J., Shlofmitz, E., 2023. Restenosis. In: StatPearls. StatPearls Publishing, Treasure Island (FL.

Restenosis: Causes, Symptoms & Treatment [WWW Document], n.d. . Cleveland Clinic. URL https://my.clevelandclinic.org/health/diseases/17132-cad-in-stent-restenosis (accessed 2.19.23)..

Ruh, D., Subramanian, S., Sherman, S., Ruhhammer, J., Theodor, M., Dirk, L., Foerster, K., Heilmann, C., Beyersdorf, F., Zappe, H., Seifert, A., 2016. Photonic sensing of arterial distension. Biomed. Opt. Express, BOE 7, 3230–3246. https://doi.org/10.1364/BOE.7.003230.

Ruth, S.R.A., Kim, M., Oda, H., Wang, Z., Khan, Y., Chang, J., Fox, P.M., Bao, Z., 2021. Post-surgical wireless monitoring of arterial health progression. iScience 24, 103079. https://doi.org/10.1016/j.isci.2021.103079.

Stefanini, G.G., Holmes, D.R., 2013. Drug-eluting coronary-artery stents. N. Engl. J. Med. 368, 254–265. https://doi.org/10.1056/NEJMra1210816.

Zhang, F., Tuck, C., Hague, R., He, Y., Saleh, E., Li, Y., Sturgess, C., Wildman, R., 2016. Inkjet printing of polyimide insulators for the 3D printing of dielectric materials for microelectronic applications. J. Appl. Polym. Sci. 133 https://doi.org/10.1002/app.43361.